Research Square

Preprints are preliminary reports that have not undergone peer review.
They should not be considered conclusive, used to inform clinical practice,
or referenced by the media as validated information.

Accurate segmentation of plant epidermal cell contours in SEM micrographs using fine-tuned Cellpose models

Jinhong Yuan
Henan Normal University
Jingyu Sun
Henan Normal University
Xinyu Wang
Henan Normal University
Jiasheng Shi
Henan Normal University
Siyuan Liu
Henan Normal University
Zhiying Yang
Henan Normal University
Chen Yang
Henan Normal University
Yingying Chang
Henan Normal University
Junhua Li
lijh@htu.cn

Henan Normal University

Research Article

Keywords: cell contour, SEM micrographs, Cellpose, fine-tuned model

Posted Date: November 9th, 2026

DOI: https://doi.org/10.21203/rs.3.rs-11378433/v1

License: This work is licensed under a Creative Commons Attribution 4.0 International License.
Read Full License

Additional Declarations: No competing interests reported.

Accurate segmentation of plant epidermal cell contours in SEM micrographs using fine-tuned Cellpose models

Jinhong Yuan, Jingyu Sun, Xinyu Wang, Jiasheng Shi, Siyuan Liu, Zhiying Yang, Chen Yang, Yingying Chang, Junhua Li*.

Engineering Research Center of Crop Genetic Improvement and Germplasm Innovation in Henan Province, College of Life Sciences, Henan Normal University, Xinxiang 453007, China

*Corresponding author. E-mail address: lijh@htu.cn (J. Li).

List of abbreviations:

SEM, Scanning electron microscope;
SE, Secondary electron;
BSE, Backscattered electron;
LM, Light microscope;
BF, Bright field;
DIC, Differential interference contrast;
GLCM, Gray-level co-occurrence matrix;
DSC, Dice similarity coefficient;
IoU, Intersection over union;
AP, Average precision.

Abstract

Background: Quantitative analysis of plant epidermal cells requires accurate segmentation of cell boundaries, a task particularly challenging for jigsaw-puzzle-shaped cells captured via scanning electron microscopy (SEM). Most existing *Arabidopsis thaliana* epidermal cell segmentation pipelines focus on light microscopy images, and current SEM segmentation workflows are largely built upon backscattered electron (BSE) micrographs. Building on these efforts, we developed Cellpose cyto3 models derived via fine-tuning for epidermal cell segmentation across plant species and imaging modalities.

Results: Here, we established a secondary electron (SE) micrograph dataset using a Coolstage system and fine-tuned the pre-trained Cellpose model cyto3 to construct specialized segmentation models. Benchmark evaluations demonstrated that our derived model achieved segmentation accuracy comparable to manual annotations, significantly outperforming the baseline cyto3 model. For *Arabidopsis* and Chinese yam, gold sputtering provided SE images with boundary contrast and segmentation accuracy that matched or surpassed those from gold-sputtered BSE imaging. The model demonstrated strong robustness to topography and image contrast variations. Cross-modality and cross-species validations confirmed that our derived model delivered reliable segmentation of epidermal cells morphologically similar to *Arabidopsis* across diverse plant species and SEM imaging modalities. Representative segmentation examples show promising visual performance from bright field, differential interference contrast and fluorescence imaging of *Arabidopsis*, as well as from cucumber and Chinese yam (abaxial epidermis), tomato and tobacco via selected modalities.

Additionally, fine-tuning cyto3 on small, domain-specific target datasets enabled accurate identification of stomatal complexes, stomatal pores, and diverse epidermal cell morphologies in monocots including maize.

Conclusions: This pipeline reduces the requirement for high contrast between cell boundaries and intracellular regions, enabling segmentation from images with relatively weak boundary contrast. Our derived cyto3 model, trained on SE-SEM topographic images, the most commonly acquired signal in SEM imaging, enables epidermal segmentation of *Arabidopsis* and generalizes to morphologically similar pavement cells. This workflow delivers a robust framework for automated leaf epidermal cell phenotyping across diverse plant species and multiple imaging modalities.

Keywords: cell contour · SEM micrographs · Cellpose · fine-tuned model

Background

Epidermal cells form the primary interface mediating interactions between plant leaves and their surrounding environment. Because epidermal morphology correlates directly with plant growth, stress tolerance, and taxonomic classification, segmenting cell contours from micrographs is essential for downstream phenotypic quantification [1]. However, imaging methods vary widely in boundary clarity, manual tracing remains labor-intensive, and many existing segmentation algorithms carry steep technical learning curves that hinder custom optimization by non-specialists. Consequently, integrating high-contrast sample preparation with accessible, adaptable segmentation tools is crucial for automated morphological profiling.

Optimized sample preparation is key to capturing distinct cell outlines. While light microscopy is widely applied in leaf epidermal studies, direct bright-field (BF) imaging of intact leaves typically yields poor boundary definition. In situ reporter-line fluorescence imaging minimizes chemical and physical disruption, producing high signal-to-noise images via confocal or light-sheet microscopy by capturing optical sections strictly from the focal plane [2]. For BF microscopy, common preparation techniques include epidermal peeling [3], chemical clearing using chloral hydrate or alkaline solutions [3, 4], and surface impression molding using nail polish, clear adhesive tape, or dental impression materials [5-7]. For scanning electron microscopy (SEM), variable-pressure SEM paired with backscattered electron (BSE) detection can capture sharp cell boundaries on uncoated leaf surfaces, bypassing traditional conductive gold or carbon coating steps [8].

High-contrast light microscopy images have driven the development of several computational tools for segmenting and measuring *Arabidopsis* pavement cells and stomata. Software platforms such as PaCeQuant, PlantSeg, MorphoGraphX, and LeafNet efficiently segment cells from confocal and light-sheet stacks [2, 9-11]. StomataCounter automates stomatal counting across differential interference contrast (DIC), BF, and SEM micrographs [12], whereas LeafNet processes both BF and confocal images. Generalist tools including Cellpose, µSAM, and MorphoLibJ offer ready-to-use segmentation pipelines [13-15]. Unlike classical tools such as PaCeQuant and MorphoLibJ that rely on hand-tuned geometric parameters, Cellpose and µSAM support lightweight model fine-tuning starting from pre-trained neural weights. Similarly, architectures like U-Net and Swin-UNet support transfer learning for high-precision phenotypic extraction [16, 17]. Nevertheless, most existing algorithms target light microscopy datasets, leaving automated boundary extraction for complex, puzzle-shaped pavement cells in SEM micrographs insufficiently addressed.

SEM images are rarely utilized for automated cell segmentation because cell borders and internal cell regions frequently display overlapping grayscale intensities. In established workflows, BSE imaging of dehydrated leaves produces bright, high-contrast boundaries across varied species. This approach relies on custom ImageJ/Fiji macros integrating the FeatureJ Hessian plugin with binary thresholding to trace pavement cells for semi-automated morphophysics [8]. Unlike dehydrated samples, which are prone to structural shrinkage and drying artifacts, fresh-frozen specimens preserve native leaf geometry while simplifying preparation [18]. Although fresh-frozen boundaries lack the bright, sharp edges characteristic of critical-point-dried BSE images, their cell outlines remain visually distinct [8]. Conventional SE detectors provide rich surface topographic detail that aids manual cell wall identification, yet standardized automated pipelines for SE-SEM cell segmentation are lacking. Current morphometric studies still depend heavily on manual ImageJ/Fiji processing [6, 8], revealing clear potential to optimize deep-learning frameworks like Cellpose for automated SEM segmentation [14].

Most existing segmentation frameworks require strong background-to-boundary contrast, such as BSE images with dark interiors and bright borders [8], single-channel fluorescent outlines [2], or peeled epidermal preparations featuring light interiors against dark cell walls [9]. In this study, we adapted Cellpose to process SE-SEM micrographs where non-boundary regions exhibit low contrast relative to cell margins. We first fine-tuned the foundational Cellpose model on internal datasets to segment complex, interlocking *Arabidopsis* pavement cells and evaluated performance directly against the default cyto3 baseline. To test model versatility across SEM modalities, we compared segmentation performance across BSE and SE images (with and without gold sputtering) from *Arabidopsis* and Chinese yam, and examined the cell morphological features best suited for the fine-tuned model (hereafter referred to as the derived model). Furthermore, we validated cross-modality generalizability using light microscopy images and extended testing to species with similar pavement cell geometries, including tomato and tobacco. Finally, we demonstrated that transfer learning on small custom datasets yields derivative models capable of isolating stomatal complexes, pores, and distinct epidermal cell types, and we discuss sample preparation strategies to optimize automated boundary extraction.

Methods

Plant material and sample preparation

Leaf epidermal tissues were sampled from indoor growth-chamber-cultivated *Arabidopsis thaliana*, tobacco (*Nicotiana benthamiana*), tomato (*Solanum lycopersicum*), and cucumber (*Cucumis sativus*). Maize (*Zea mays*) leaves were collected from the experimental field of Henan Normal University (35.3216° N, 113.9147° E), and Chinese yam (*Dioscorea polystachya*) was obtained from the Wenxian Institute of Agricultural Sciences, Jiaozuo (34.947415° N). All leaf tissues were excised, avoiding primary veins. Dehydrated SEM samples were fixed, dehydrated, and t-butanol freeze-dried [7]. BF samples were prepared via epidermal peeling, nail polish surface imprinting, or chloral hydrate clearing. Fluorescent samples were generated through *Agrobacterium*-mediated transient transformation of tobacco leaves with minor modifications from Yang et al. [19].

Microscopic imaging

Fresh leaf samples were frozen and observed under a tabletop SEM (Hitachi TM3030Plus, Japan) equipped with a Peltier stage (Deben MK3 Coolstage, UK). Coolstage imaging used a SE detector at 5 kV, as BSE imaging produced uninformative micrographs and 5 kV enhanced surface topographic details. Dehydrated samples were gold-sputtered for 0–240 s in a KYKY SBC-12 ion coater before imaging under either SE or BSE modes at 50–70 Pa vacuum to evaluate sputtering effects. Sample preparation followed previously published methods [7]. Slide preparation and imaging adjustments were applied to other sample types to optimize surface contour visibility. BF imaging was performed on a Leica DMIL inverted microscope or a Leica TCS SP8 confocal microscope operated in DIC mode. Plasma membrane-localized GFP signals outlining cell boundaries were visualized using the confocal microscope.

Construction and evaluation of derived Cellpose models

A total of over 300 images (14–648 pavement cells per image) were manually annotated, and hundreds of additional supporting micrographs were also included in this study. Two microscopic datasets comprising SEM and light microscopy images were assembled. The primary training dataset contained 26 Coolstage SEM micrographs of *Arabidopsis* leaves (400–1000× magnification), each containing 14–84 annotated epidermal cells, and was used to fine-tune the baseline cyto3 model. An independent test dataset of 68 SEM images (38 Coolstage-fixed and 30 dehydrated *Arabidopsis* samples) was used for model evaluation. For broader cross-modality testing, BF micrographs (including DIC) of *Arabidopsis* and cucumber leaves were collected across three preparation types (peeled epidermis, chemically cleared tissue, and nail polish impressions) using 20× and 40× objectives. Additional training datasets included BF micrographs of peeled or cleared maize leaves, and a supplementary set of 61 SEM micrographs (400–1200×) from abaxial leaf surfaces of *Arabidopsis*, cucumber, and Chinese yam, comprising 28 images of stomatal complexes and 33 of stomatal pores. These independent datasets were used to train customized derivative models from the pre-trained Cellpose cyto3 architecture.

Cell outlines were manually annotated across all training images. Each sample entry was organized into four linked files: the raw image input, a PNG/TIF annotation mask, an outline file, and an NPY file storing boundary coordinates. Cells truncated at image edges were retained, and the image border defined their boundaries for segmentation evaluation. Standardized datasets were imported into Cellpose 3.1.0 using the pre-trained cyto3 weights as the base model. Training was conducted with an initial learning rate of 0.1, default parameter configurations, and iterative training over 400–1000 epochs to ensure fit convergence while preventing overfitting. Segmentation performance was quantified using intersection over union (IoU), dice similarity coefficient (DSC), and average precision (AP, AP=TP/(TP+FN+FP) for cell instances) [14, 20, 21]. IoU was determined as the intersection divided by the union area between predicted and manually annotated masks. DSC was the overlap between prediction and ground truth. AP was computed across a range of IoU matching thresholds for cell-instance matching, where TP, FP, and FN represent the counts of true-positive, false-positive, and false-negative cell instances, respectively.

Morphological profiling and statistical analysis

To quantify differences in *Arabidopsis* cell images under various imaging conditions, we measured gray values and gray-level co-occurrence matrix (GLCM) texture features (correlation, homogeneity) [22, 23] for cell outlines and intracellular regions. We tested five imaging conditions,

with five replicate images per condition; we sampled 2000 points from the outlines and inner non-contour regions of each image for gray-value calculation. External reference images were obtained from published literature and datasets: BSE images from Talbot and White [8] were cropped from Figs. 2C, 3A, 4C, 5A, and 10; LeafNet dataset images were cropped from Figs. 1A, 3A, 4B, 5A, and S1A brightfield images for comparison [9]. External reference images had compression artifacts and were used only as controls for intergroup comparison.

Automated cell segmentation was executed in Cellpose to generate binary masks. Masks were imported into Fiji/ImageJ, and individual cells were isolated with the Label ROI tool in the MorphoLibJ plugin to create label maps. Representative cells ($n \geq 30$ per group; mean = 76, range: 48–126) were evaluated for four morphological descriptors on adaxial and abaxial leaf surfaces of *Arabidopsis*, cucumber, and Chinese yam. Solidity and circularity were measured using Fiji's Analyze Particles module, geodesic elongation was calculated in MorphoLibJ [13], and lobe counts were quantified following PaCeQuant definitions [2]. Geodesic elongation is defined as D_g/D_{ins}, where D_g is geodesic diameter, and D_{ins} is the diameter of the largest inscribed circle. A value of 1 indicates a circular cell; larger values correspond to elongated or convoluted outlines [24]. Parameter feature importance was further assessed using IBM SPSS Modeler 18.0.

Accelerating voltage comparisons (5 kV *vs*. 15 kV) showed no significant effect on segmentation accuracy in *Arabidopsis*, though minor variations occurred in Chinese yam due to surface epicuticular deposits that blurred boundary contrast. Consequently, voltage groups were pooled for final statistical comparisons. Experiments included six biological replicates, sampling 2–3 fields of view per replicate and 38–88 cells per statistical group. One-way ANOVA or Student's *t*-tests were performed for multi-group and two-group comparisons, respectively, with Tamhane's T2 post-hoc test applied when variance homogeneity was violated ($P < 0.05$). Statistical analyses were run in IBM SPSS Statistics 27, and figures were generated using GraphPad Prism 9 and SigmaPlot 10.0.

Results

Characteristics of SE and BSE imaging modes

Following drying and gold sputtering, SEM micrographs of cucumber and *Arabidopsis* leaf samples were collected using a BSE detector (Figure 1A, D). In BSE mode, non-boundary cell regions exhibit uniform topography. Grayscale variation in BSE micrographs reflects local atomic composition: cell walls accumulate cations such as Ca and K, with the middle lamella specifically enriched in pectin-bound calcium, generating strong backscattered signals that appear as bright cell outlines [8]. Conversely, non-boundary regions comprise single cell wall layers and sparse organelles, yielding weak BSE signals that remain homogeneously dark. Dehydrating SEM specimens further concentrates wall-bound ions, widening the signal contrast between the middle lamella and internal cell surfaces [25].

To understand why segmentation of our SEM epidermal cells was difficult, we examined the imaging characteristics underlying SE-SEM images. Unlike BSE contrast, SE brightness depends on secondary electron yield, which is dictated by surface topography and microstructural variation. Gray value analysis revealed no, or only small, differences between cell outlines and intracellular regions under our imaging conditions (Figure S1A, right), compared with the large, high-contrast differences observed in the published images (Figure S1A, left). Visual inspection of the BSE images [8] and BF images [9] revealed relatively uniform intracellular backgrounds. In SE imaging, cell boundaries remain distinguishable from adjacent regions (Figure 1B–C, E–F), whereas non-

boundary regions show prominent topographic fluctuations rather than a uniform background. Dehydration of SEM leaf specimens frequently causes cell collapse and surface wrinkling [7]; the resulting topographic artifacts distorted boundary edges and obscured true cell morphology (Figure 2B, E).

We further used GLCM correlation and homogeneity metrics to quantify intracellular texture characteristics of *Arabidopsis* epidermal cells. Intracellular GLCM correlation values were higher for SE-SEM topographic images (Coolstage and dehydrated samples) than for BSE images (from the literature and this study), indicating more continuous, gradual grayscale variation between adjacent pixels. GLCM homogeneity analysis showed that the gray spatial distribution features of dehydrated-leaf SE-SEM images differed significantly from other imaging conditions in this study and external reference images. Consistent with visual observation, cells in Coolstage and dehydrated-leaf SEM images displayed darker centers with grayscale gradually brightening toward cell boundaries (Figure 1).

Young leaves rapidly lose moisture and deform under SEM vacuum conditions. Treating samples with cryoprotectants for Coolstage observation extends imaging stability [26] and prevents dehydration-induced shrinkage. Here, cryoprotectant-treated leaves [7] imaged on a Coolstage using an SE detector at 5 kV yielded intact, clear pavement cell outlines. Conversely, switching to BSE mode failed to resolve cell borders or surface topography in *Arabidopsis*, tomato, and tobacco, producing featureless images unsuitable for boundary tracing. Such contrast behavior also exhibits species-specific variation: even under SE detection, species with thick epicuticular wax coatings (e.g., Chinese yam) fail to yield sharp cell boundaries (images not shown).

Talbot and White [8] developed a semi-automated image segmentation macro within Fiji. When applied to high-contrast BSE micrographs, this workflow efficiently extracts epidermal contours and accelerates morphometric analysis. However, experimental variations in electron microscope hardware, specimen preparation, and acquisition settings compromise image consistency (Figure S1). When applied to SE-SEM micrographs of gold-sputtered leaves (Figure 1), this Fiji macro generates false outlines in high-noise regions (Figure S2A–B, D–E) while producing broken or missing boundaries where local signal intensity drops (Figure S2E, F). Furthermore, genuine wall features were frequently misidentified as artifacts and removed by the PruneAll function, inappropriately merging discrete adjacent cells.

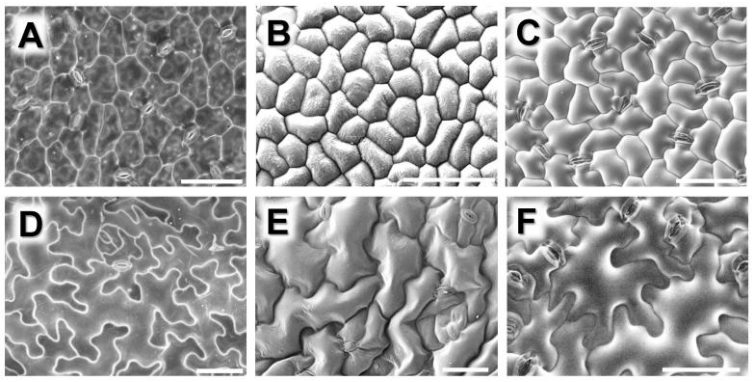


Figure 1. SEM micrographs of leaf epidermis acquired in BSE and SE modes
A–C: cucumber; D–F: *Arabidopsis*. Images A and D were captured using a backscattered electron (BSE) detector; B, C, E, and F were acquired using a secondary electron (SE) detector. Micrographs C and F depict fresh leaf samples; all other panels show dehydrated specimens. Scale bars = 50 μm.

Pavement cell segmentation using Cellpose cyto3

To identify a segmentation platform compatible with variable imaging modalities, we evaluated Cellpose across diverse sample preparations using its built-in cyto3 model. Model performance was tested on adaxial and abaxial leaf epidermises from *Arabidopsis*, cucumber, and Chinese yam (*Dioscorea*). On SE-SEM images featuring puzzle-shaped *Arabidopsis* pavement cells with pronounced undulations (Figure 1E–F), cyto3 either severely under-segmented or completely failed to detect most cell boundaries.

For convex-shaped adaxial epidermal cells in cucumber and Chinese yam, the default cyto3 model achieved high segmentation accuracy (Figure 2A, B). Conversely, abaxial epidermal cells of these two species and *Arabidopsis* epidermal cells featuring wavy outlines were poorly segmented (Figure 2). Performance discrepancies correlated strictly with boundary geometry rather than specimen preparation (dehydrated *vs*. Coolstage) or detector type (BSE *vs*. SE).

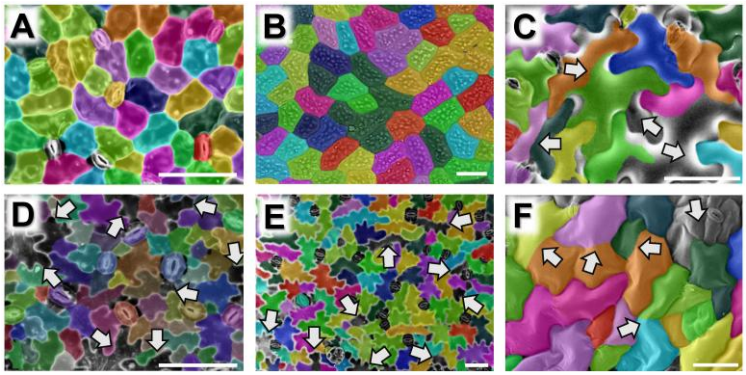


Figure 2. Segmentation of leaf pavement cells using the default Cellpose cyto3 model.
A, D: adaxial and abaxial epidermis of cucumber leaves; B, E: adaxial and abaxial epidermis of *Dioscorea* leaves. Images were acquired in BSE-SEM mode; panels show corresponding segmentation masks. White arrows highlight poorly segmented epidermal cells. C, F: segmentation outputs corresponding to Figure 1F and 1E, respectively. Scale bars = 50 μm.

Development and validation of the derived Cellpose model

To resolve the poor accuracy of default cyto3 on *Arabidopsis* pavement cells in SEM micrographs, we assembled a training dataset of 26 Coolstage SE-SEM images containing 443 manually annotated intact cells. Fine-tuning pre-trained cyto3 weights on this dataset yielded a customized derived model.

Quantitative performance evaluations are summarized in Figure 3. Segmentation quality was assessed using the DSC, measuring spatial mask overlap against manual ground truth [20], and AP, evaluating single-cell instance detection accuracy [14]. Figure 3A outlines detected cell counts across varying IoU thresholds [21], while Figure 3B and 3C present DSC and AP distributions, respectively. Gamma distribution fits and cell area profiles are shown in Figure 3D and 3E. The derived model consistently matched manual annotations and significantly outperformed baseline cyto3 in DSC and AP scores. In cell area profiling (Figure 3F), the derived model delivered significantly higher quantification fidelity than the original cyto3.

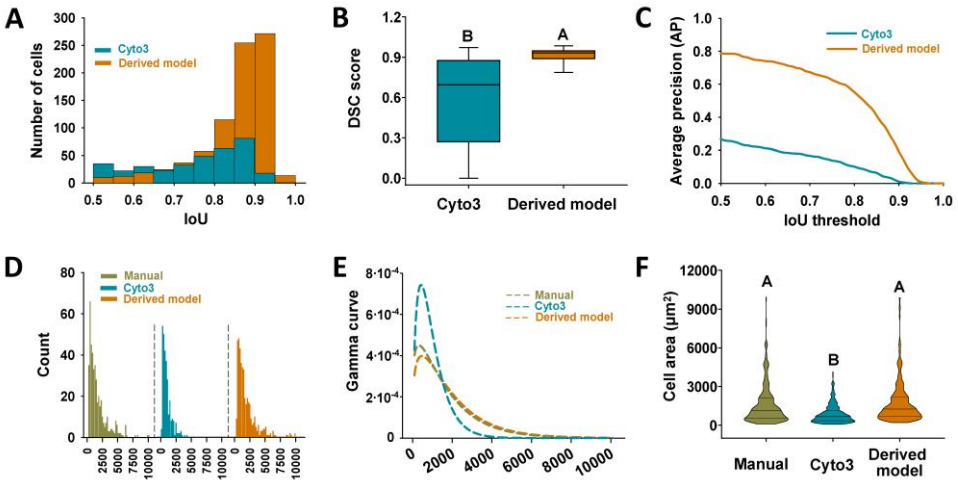


Figure 3. Segmentation accuracy of the derived model compared with baseline cyto3.

A, Detected cell counts across varying Intersection-over-Union (IoU) thresholds. B, Dice similarity coefficient (DSC) values relative to manual ground truth. C, Average precision (AP) comparison between baseline cyto3 and the derived model. D, Cell area frequency distributions for manual annotations, original cyto3, and the derived model. E, Fitted gamma distribution curves across all three groups. F, Violin plots showing cell area distributions (solid line: median; dotted lines: first and third quartiles; width: probability density). Distinct capital letters indicate significant differences at $P < 0.01$.

Evaluation of derived model performance

The derived cyto3 derived model effectively adapted across diverse imaging conditions, including SE images of dehydrated *Arabidopsis* (Figure 4C) and Coolstage cucumber epidermises (Figure 4F), as well as BSE images of dehydrated *Arabidopsis*, cucumber, and Chinese yam samples (segmentation masks for Figs. 1 and 2 omitted). Default cyto3 missed numerous cells and produced severe under-segmentation (Figure 4B, E). Conversely, the derived model consistently yielded accurate cell boundaries for dehydrated *Arabidopsis* (Figure 4F) and resolved complete contours across the lower cucumber epidermis (Figure 4C). For complex, interlocking pavement cells, the derived model demonstrated superior accuracy compared to cyto3, maintaining robust performance regardless of sample pretreatment (Coolstage vs. dehydrated) or detection mode (SE vs. BSE).

We benchmarked the derived model against default cyto3 using an independent test set of 68 SEM images containing both Coolstage-fixed and dehydrated *Arabidopsis* samples. The derived model achieved a substantially higher DSC (0.81 *vs*. 0.59) than cyto3, confirming greater spatial overlap with manual ground truth (Figure 4G). Compared with the baseline cyto3 model, the derived model yields better segmentation performance on SEM images from both Coolstage-treated and dehydrated specimens. The AP@0.5 for Coolstage samples (0.71) exceeded that of dehydrated samples (0.59). This difference is attributable to local collapse and wrinkling, commonly observed in dehydrated specimens [18, 27]. These findings confirm that targeted fine-tuning on modest datasets significantly elevates segmentation accuracy for complex SEM epidermal micrographs.

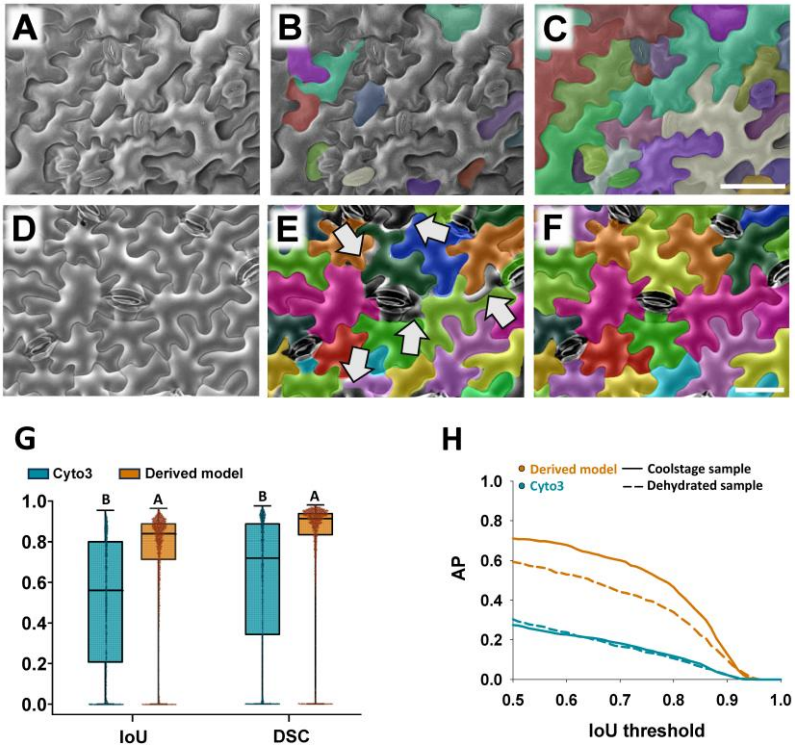


Figure 4. Performance comparison between default Cellpose cyto3 and the derived derived model. A–C: SEM micrographs of dehydrated *Arabidopsis* leaf epidermis; D–F: fresh cucumber leaf epidermis. Panels B and E show default cyto3 segmentations; C and F display derived model outputs. Arrows highlight poorly segmented boundaries. G: Quantitative performance evaluation showing IoU scores and DSC scores. F: Comparison of AP scores between the baseline cyto3 and derived model for image segmentation of Coolstage-treated samples and dehydrated SEM samples. Scale bars = 50 μm.

Model robustness across sputtering durations and detection modes

Dehydrated *Arabidopsis* and Chinese yam epidermal samples were evaluated across six gold-sputtering durations: 0 s (uncoated controls), 40 s, 80 s, 120 s, 160 s, and 240 s (Figs. 5 and 6). Because convex Chinese yam pavement cells were already segmented adequately by default cyto3, detailed model comparisons were conducted on *Arabidopsis* specimens (Figure 5).

The derived model improved segmentation fidelity across both adaxial and abaxial *Arabidopsis* surfaces, achieving significantly higher DSC scores than cyto3 (Figure 5G). It also displayed enhanced stability across detector modes and sputtering times. Owing to this high robustness, *Arabidopsis* BSE and SE images yielded equivalent segmentation quality regardless of coating duration. Conversely, when evaluating the baseline cyto3 model on SE images, gold sputtering was necessary to match BSE performance, peaking at 80 s sputtering before declining at 240 s (Figure 6G), as uncoated SE images lacked sufficient boundary contrast (Figure 6A).

The impact of gold sputtering varied by species, even though surface topographical definition improved in both *Arabidopsis* and Chinese yam SE micrographs (Figs. 5B–C and 6C). While the derived model eliminated performance gaps between BSE and SE imaging in *Arabidopsis*, Chinese yam required gold sputtering to maximize segmentation accuracy in both modes. For abaxial Chinese yam surfaces, DSC scores showed an overall upward trend with increasing coating time, outperforming uncoated specimens across both epidermal sides (Figure 6A–F).

BSE segmentation quality was strongly species-dependent. In uncoated dehydrated samples, *Arabidopsis* cell boundaries appeared far sharper in BSE mode than those of Chinese yam. Across all sputtering durations, *Arabidopsis* BSE micrographs maintained high contrast between cell walls

and internal regions (Figure 5D). In contrast, uncoated Chinese yam BSE images exhibited faint, indistinct contours (Figure 6D–E) that were difficult to trace even visually, corresponding to the lowest recorded DSC values at 0 s (Figure 6G).

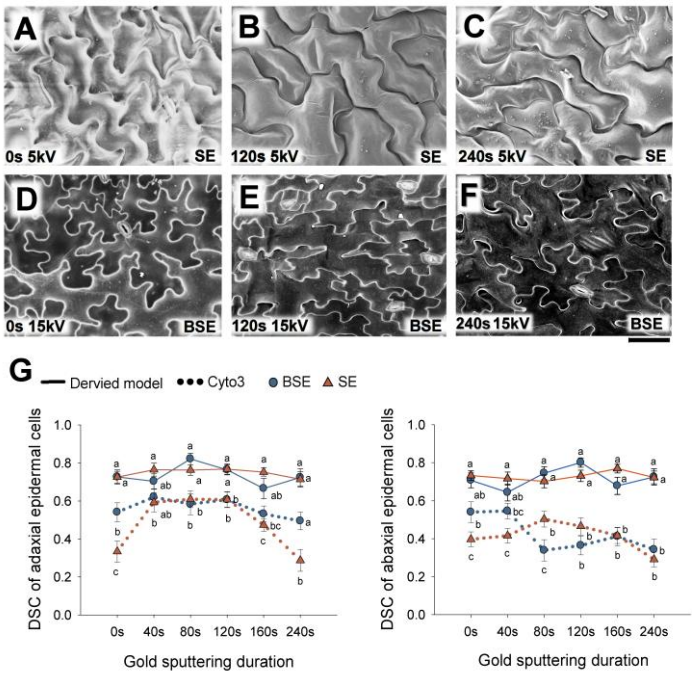


Figure 5. Derived model performance on dehydrated *Arabidopsis* leaf micrographs
A–C: Secondary electron (SE) detector images; D–F: Backscattered electron (BSE) detector images. Sputtering duration and accelerating voltages (5 kV, 15 kV) are indicated in image corners. G: Quantitative DSC comparisons between the derived model and cyto3 relative to ground truth. Distinct lowercase letters indicate significant differences ($P < 0.05$). Scale bars = 50 μm.

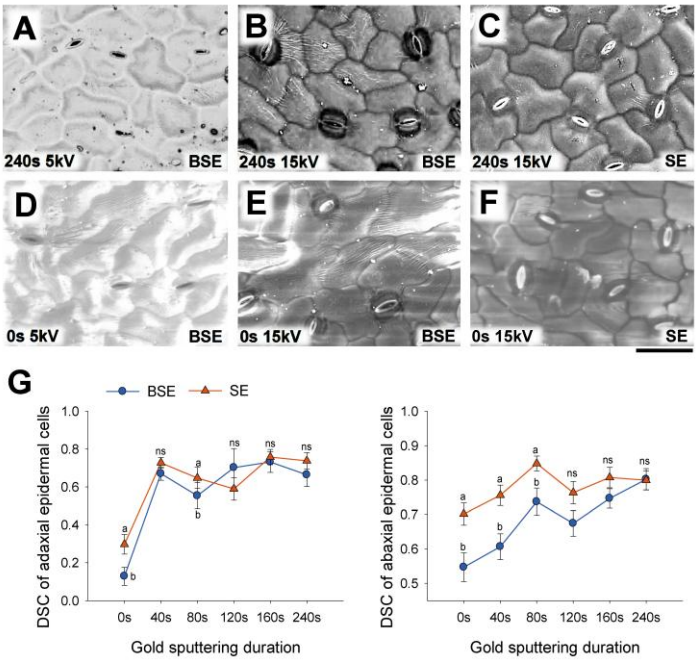


Figure 6. Segmentation performance comparison between BSE and SE modes on Chinese yam epidermis.
A–C: Specimens sputter-coated for 240 s; D–F: Uncoated controls (0 s). 5 kV and 15 kV denote accelerating voltages. G: DSC performance of the derived model across BSE and SE modes relative to ground truth. Distinct lowercase letters denote significant differences ($P < 0.05$). Scale bars = 50 μm.

Morphological variation and candidate features associated with segmentation performance

To identify geometric traits favoring the derived model, 622 adaxial and abaxial epidermal cells from *Arabidopsis*, cucumber, and Chinese yam were evaluated for solidity, circularity, geodesic elongation, and lobe count. Each cell was categorized by whether it was better segmented by the derived model or default cyto3. Random forest feature importance ranking identified geodesic elongation as the primary morphological parameter governing model superiority among these four traits, with a combined importance index of 0.90.

Morphological trait distributions varied substantially among the three species (Figure 7). *Arabidopsis* cells were highly elongated, displaying the lowest solidity and circularity values. Within *Arabidopsis*, adaxial cells were relatively compact, whereas abaxial cells exhibited pronounced puzzle-piece geometries with elevated lobe counts and lower solidity. Cucumber and Chinese yam showed clear adaxial–abaxial dimorphism: adaxial cells were convex with few lobes, whereas abaxial cells formed interlocking patterns characterized by higher geodesic elongation and reduced solidity. Chinese yam exhibited the lowest overall geodesic elongation, corresponding to short, stout cell proportions, and the highest solidity and circularity values, reflecting rounded, compact cell contours.

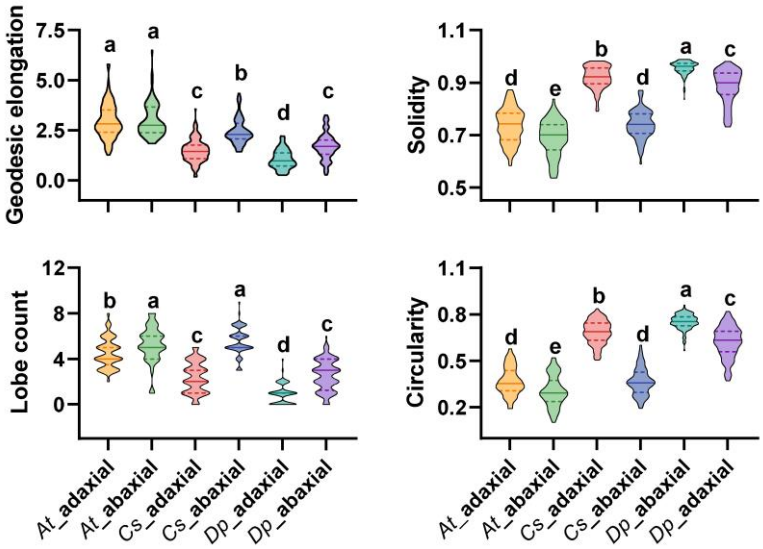


Figure 7. Quantitative phenotypic profiling of pavement cell geometry.
Note: *At: Arabidopsis thaliana; Cs: Cucumis sativus* (cucumber); *Dp: Dioscorea polystachya* (Chinese yam). Distinct lowercase letters indicate significant differences ($P < 0.05$).

Cross-modality applications and strategic considerations

Application to light microscopy data. Built upon the Cellpose framework, the derived model enables single-click automated segmentation through a graphical interface, offering high stability and broad generalizability (Figure 8). It accurately resolves leaf epidermal contours in both *Arabidopsis* and cucumber across three standard light microscopy preparations: direct epidermal peeling (Figure 8C), nail polish imprinting (Figure 8G), and chloral hydrate clearing (Figure 8K). While the standard Fiji processing macro and baseline cyto3 model display limited adaptability to light microscopy datasets, the derived model delivers consistent segmentation across all preparation types, including peeled cucumber abaxial epidermis (Figure 8A), nail polish impressions of *Arabidopsis* leaves (Figure 8E), and cleared cucumber abaxial surfaces (Figure 8I). *Arabidopsis* pavement cells exhibit wide size disparities, varying up to 95.6–fold in area (Figure 3D). Operating the interface with a single fixed default diameter can cause minor under-detection of unusually large

or small cells; adjusting this parameter manually restores full boundary recovery. Furthermore, integrating code-based adaptive diameter estimation automates size adjustments in a single pass, maximizing overall segmentation fidelity (Figure 8D, H, L).

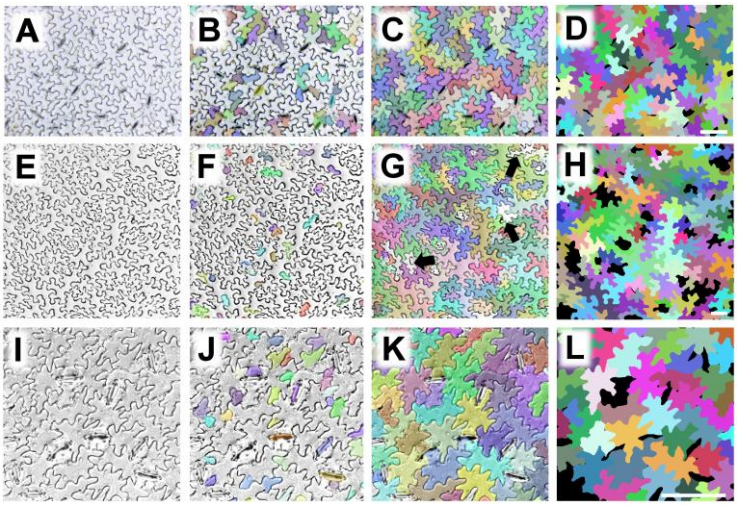


Figure 8. Enhanced epidermal cell segmentation in light micrographs using the derived model
A, E, I: Raw light micrographs of leaf epidermis; B, F, J: Baseline Cellpose cyto3 segmentations; C, G, K: Derived model results; D, H, L: Outputs following adaptive diameter optimization. A–D: Peeled cucumber epidermis imaged under inverted bright-field microscopy; E–H: Nail polish impressions of *Arabidopsis* epidermis captured via confocal DIC; I–L: Cleared cucumber epidermis imaged via confocal DIC. Arrows highlight cells unsegmented under a uniform GUI diameter setting. Scale bars = 50 μm (shown in D, H, and L for respective rows).

Extension to diverse species, tissues, and specialized structures. The derived model generalizes successfully to Coolstage SEM micrographs of tomato (Figure 9A) and tobacco leaves (data not shown), whose pavement cells share the complex, puzzle-piece geometries characteristic of *Arabidopsis*. Across all three species, adaxial cells remain more compact than their abaxial counterparts. Figure 9A illustrates precise boundary extractions on tomato adaxial epidermis, and Figure 9C demonstrates robust segmentation on fluorescently labeled tobacco epidermal membranes.

Concurrently segmenting pavement cells alongside stomatal complexes often causes stomatal misclassification when guard cells differ markedly in scale or border contrast from surrounding pavement cells. To resolve stomata and measure pore dimensions, we trained specialized derivative models on focused SEM datasets acquired in SE or BSE modes. These custom models accurately isolated stomatal pores in Chinese yam and enabled precise stomatal apparatus measurements in *Arabidopsis* (Figure 9B). Similarly, fine-tuning cyto3 on light microscopy datasets from maize yielded highly accurate segmentations of monocot epidermal files (Figure 9D). Comparable segmentation performance was also achieved for rice epidermal light microscopy images (data not shown).

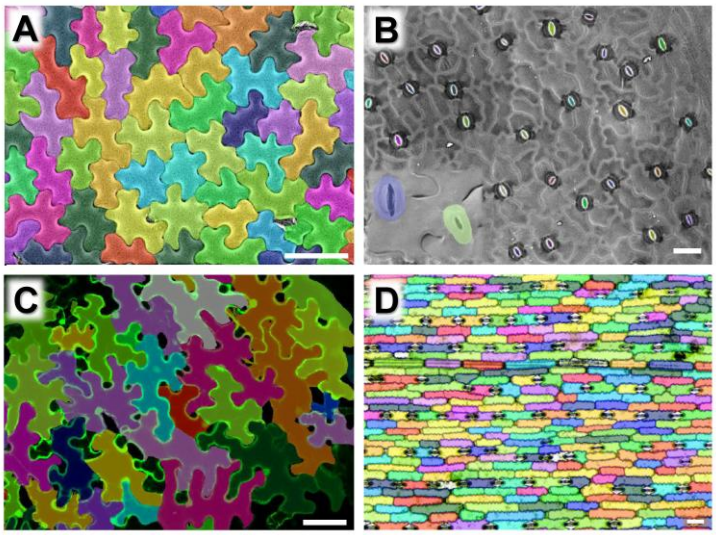


Figure 9. Specialized applications of derived cyto3-derived models.
A and C, Cell segmentations on tomato Coolstage SEM micrographs and tobacco leaf fluorescence images, respectively. B, Specialized cyto3 derivative models isolated stomatal pores in Chinese yam leaf epidermis and quantified stomatal complexes in *Arabidopsis* (bottom-left region; not an enlarged inset). D, Segmented maize leaf epidermal files. Scale bars = 50 μm.

Discussion

Traditional optical microscopy workflows and BSE-SEM processing macros rely on sharp, unambiguous cell boundaries and high topographic uniformity for reliable segmentation. In contrast, SE micrographs capture subtle topographic relief through depth-of-field variations, frequently introducing non-uniform backgrounds. In transmitted light microscopy, excessive specimen thickness or variable sample depth compromises optical clarity. Fluorescence imaging often requires multi-plane Z-stack projections that complicate acquisition workflows, while weak fluorophore signals severely degrade boundary tracing [2, 8, 9]. Quantitative comparisons with literature and dataset images further showed that our SE images had lower grayscale contrast at cell boundaries and within cells but provided richer surface topographical information (Figure S1), which contributed to the segmentation challenges addressed in this study.

For automated BSE micrograph analysis, Talbot and White [8] introduced a macro that extracts cell wall skeletons and removes artifactual branches via a custom function named PruneAll. However, when applied to our gold-sputtered BSE micrographs, the macro performed poorly, corroborating earlier reports that gold sputtering attenuates intrinsic contrast between middle lamellae and cell interiors [8]. Conversely, deep-learning models built on Cellpose tolerate BSE images with lower contrast. Provided that local cell wall boundaries maintain adequate definition, moderate contrast in outlines and cell interiors can be accommodated during single-cell instance segmentation, expanding the operational range of SEM imaging settings and sample preparation protocols.

Because BSE imaging relies on atomic-number contrast, it is rarely selected for routine plant morphological characterization. Due to fundamental signal differences between BSE and SE modes, automated processing tools built for BSE data fail to maintain stable boundary detection when applied to SE micrographs, constraining the utility of traditional Fiji-based macros. Here, we leveraged standard SE imaging to capture rich surface topography with extended depth of field, establishing an optimized deep-learning workflow. Unlike prior algorithms restricted to single

imaging modalities [2, 8, 11], our derived model processes heterogeneous datasets from both light and electron microscopy. It achieves accurate, stable pavement cell segmentation across SE, BSE, BF, DIC and fluorescence micrographs, showing robustness to variations in topography and image contrast and offering a flexible platform for plant phenotypic profiling across diverse imaging hardware.

Although derived models do not require sharply defined outlines, achieving high segmentation accuracy still requires sufficient local boundary contrast. Optimizing sample preparation, selecting appropriate SE/BSE detectors, and fine-tuning accelerating voltage and vacuum levels improve outline sharpness [8], minimizing image artifacts caused by specimen variation, hardware differences, or improper acquisition settings. A modest dataset is adequate for cyto3 fine-tuning and may be built from multiple imaging modalities including BF, DIC, SE or BSE images. High-quality data with clear contours and low noise comes from optimized sample preparation and imaging conditions, which vary by sample type. For maize, the SEM images exhibited weak grayscale contrast between cell outlines and intracellular regions compared to BF images [7]; therefore, only BF images were used for model training. When training for stomatal complexes and stomatal pores, stomatal structures are prone to deformation under Coolstage SEM conditions [7]. Accordingly, fixed and dehydrated SEM specimens produce superior segmentation results compared with Coolstage samples.

Our derived model automates *Arabidopsis* pavement cell boundary extractions with accuracy matching manual annotations. When target structures vary widely in size or contrast, such as small stomata embedded within large pavement cells [28], training dual-purpose models can lead to stomatal misclassification. Dedicated models trained exclusively on stomatal images resolve guard cell boundaries and pore dimensions cleanly. Minor segmentation errors can be adjusted post-processing using built-in interactive tools. Output masks import seamlessly into ImageJ/Fiji for downstream morphometric analysis via established tools like MorphoLibJ, PaCeQuant, or MorphoGraphX, facilitating studies on cell development, morphogenesis, and mutant phenotypes [2, 11, 13]. By removing the need for extreme image contrast [8, 9] and requiring only modest training datasets, this fine-tuning approach lowers technical barriers, delivering an accessible, high-throughput quantitative solution for plant cell biology.

Supplementary Figures

Supplementary Figure S1. Comparison of gray values and GLCM parameters in *Arabidopsis* epidermal cell images.

Supplementary Figure S2. Cell contour segmentation performance of the BSE-Fiji pipeline on SEM micrographs.

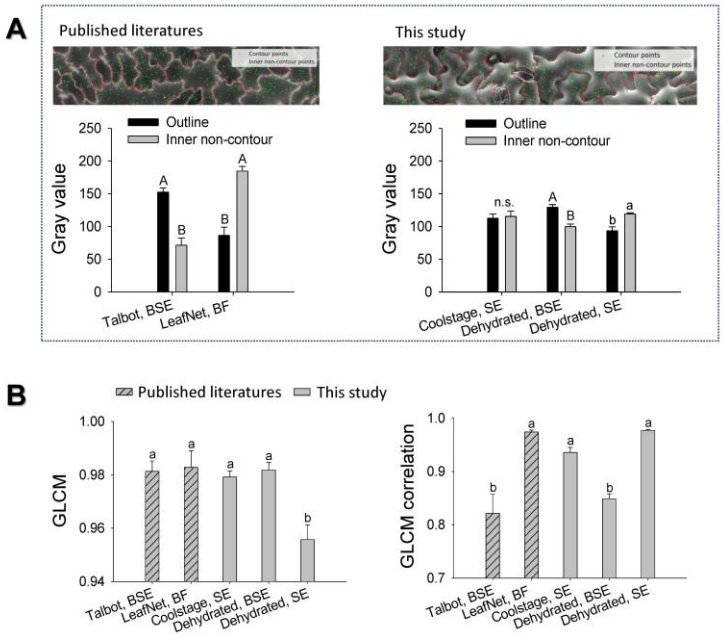


Figure S1. Comparison of gray values and GLCM parameters in *Arabidopsis* epidermal cell images. (A) Representative micrographs and quantified gray values of cell outlines and inner non-contour regions from published literature (left) and this study (right). Published reference images were acquired under variable-pressure BSE [27, samples either uncoated or carbon-coated] and brightfield microscopy [9]. Images from this study (right) were collected under varied SEM conditions: Coolstage and dehydrated samples imaged with BSE (gold-sputtered) and SE modes. (B) GLCM homogeneity (left) and GLCM correlation (right) calculated for images from published datasets and this study.

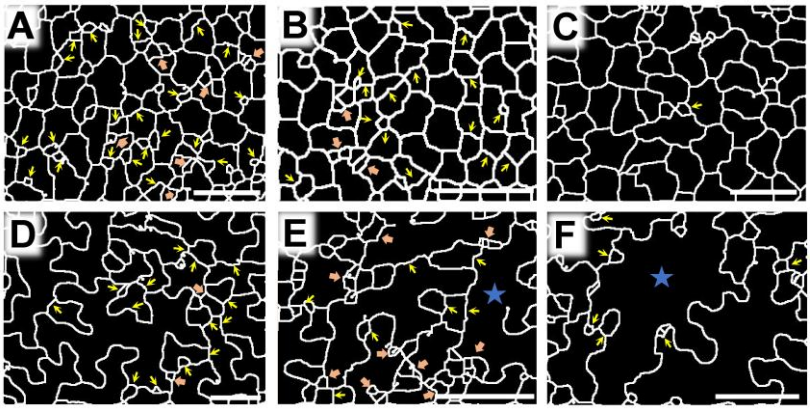


Figure S2. Cell contour segmentation performance of the BSE-Fiji pipeline on SEM micrographs. (A–F) Paired SEM images and corresponding segmentation outputs generated using the workflow established by Talbot and White [8]. Thin yellow arrows highlight over-segmented cell outlines; thick orange arrows indicate localized over-segmentation; blue stars mark missing boundary segments resulting from automated contour pruning.

Declarations

Ethics approval and consent to participate

Not applicable.

Consent for publication

Not applicable.

Availability of data and materials

For peer review purposes, testing instructions and a representative subset of 15 *Arabidopsis* leaf SEM micrographs are provided. This subset was selected from the 68-image testing dataset to cover diverse epidermal cell morphologies, using different sample preparation methods (Coolstage-prepared samples, dehydrated samples) and detectors (backscattered electron detector, secondary electron detector). Corresponding manually annotated segmentation files are supplied for these images. If this manuscript is accepted, the full dataset and all model weights associated with this work will be deposited in an open public repository.

Competing interests

The authors declare that they have no competing interests.

Funding

This study was supported by the National Natural Science Foundation of China (Grant Nos. 31970380 and U1504319), the Natural Science Foundation of Henan (Grant No. 252300420202), and Key Scientific Research Projects of Universities in Henan Province (24A180015).

Authors' Contributions

Conceived and designed the experiments: Jinhong Yuan and Junhua Li. Performed the experiments: Jinhong Yuan, Jingyu Sun, Xinyu Wang, Zhiying Yang, Chen Yang. Analyzed the data: Jinhong Yuan Xinyu Wang, Jiasheng Shi, Siyuan Liu, Yingying Chang. Drafted and revised manuscript: Jinhong Yuan, Junhua Li, and Jingyu Sun. All authors read and approved the final manuscript.

Acknowledgments

We highly appreciate the expertise and comments of the reviewers who helped us improve the quality of the manuscript. We would like to express our sincere gratitude to Xiaofei Liu (College of Life Sciences, Henan Normal University) for providing the fluorescence images used in this study.

References

1. Zhang F, Wang B, Lu F, Zhang X: **Rotating stomata measurement based on anchor-free object detection and stomata conductance calculation**. *Plant Phenom* 2023, **5**:0106.
2. Möller B, Poeschl Y, Plötner R, Bürstenbinder K: **PaCeQuant: A tool for high-throughput quantification of pavement cell shape characteristics**. *Plant Physiol* 2017, **175**(3):998-1017.
3. Pantaleno R, Schiel P, García-Mata C, Scuffi D: **Analysis of guard cell readouts using *Arabidopsis thaliana* isolated epidermal peels**. *Bio Protoc* 2024, **14**(14):e5033.
4. Morawetz JJ: **A clearing protocol for whole tissues: An example using haustoria of Orobanchaceae**. *Appl Plant Sci* 2013, **1**(1).
5. Kusumi K: **Measuring Stomatal Density in Rice**. *Bio Protoc* 2013, **3**(9):e753.
6. Wu HC, Huang YC, Liu CH, Jinn TL: **Using silicon polymer impression technique and scanning electron microscopy to measure stomatal aperture, morphology, and density**. *Bio Protoc* 2017, **7**(16):e2449.
7. Yuan J, Wang X, Zhou H, Li Y, Zhang J, Yu S, Wang M, Hao M, Zhao Q, Liu L *et al*: **Comparison of sample preparation techniques for inspection of leaf epidermises using light microscopy and scanning electronic microscopy**. *Front Plant Sci* 2020, **11**:133.
8. Talbot MJ, White RG: **Cell surface and cell outline imaging in plant tissues using the backscattered electron detector in a variable pressure scanning electron microscope**. *Plant Methods* 2013, **9**(1):40.
9. Li S, Li L, Fan W, Ma S, Zhang C, Kim JC, Wang K, Russinova E, Zhu Y, Zhou Y: **LeafNet: a tool for segmenting and quantifying stomata and pavement cells**. *Plant Cell* 2022, **34**(4):1171-1188.
10. Wolny A, Cerrone L, Vijayan A, Tofanelli R, Barro AV, Louveaux M, Wenzl C, Strauss S, Wilson-Sánchez D, Lymbouridou R *et al*: **Accurate and versatile 3D segmentation of plant tissues at cellular resolution**. *eLife* 2020, **9**:e57613.
11. Barbier de Reuille P, Routier-Kierzkowska A-L, Kierzkowski D, Bassel GW, Schüpbach T, Tauriello G, Bajpai N, Strauss S, Weber A, Kiss A *et al*: **MorphoGraphX: A platform for quantifying morphogenesis in 4D**. *eLife* 2015, **4**:e05864.
12. Fetter KC, Eberhardt S, Barclay RS, Wing S, Keller SR: **StomataCounter: a neural network for automatic stomata identification and counting**. *New Phytol* 2019, **223**(3):1671-1681.
13. Legland D, Arganda-Carreras I, Andrey P: **MorphoLibJ: integrated library and plugins for mathematical morphology with ImageJ**. *Bioinformatics* 2016, **32**(22):3532-3534.
14. Stringer C, Pachitariu M: **Cellpose3: one-click image restoration for improved cellular segmentation**. *Nat Methods* 2025, **22**(3):592-599.
15. Archit A, Freckmann L, Nair S, Khalid N, Hilt P, Rajashekar V, Freitag M, Teuber C, Spitzner M, Tapia Contreras C *et al*: **Segment anything for microscopy**. *Nat Methods* 2025, **22**(3):579-591.
16. Ronneberger O, Fischer P, Brox T: **U-Net: Convolutional networks for biomedical image segmentation**. In*: 2015; Cham*. Springer International Publishing: 234-241.
17. Cao H, Wang Y, Chen J, Jiang D, Zhang X, Tian Q, Wang M: **Swin-Unet: Unet-like pure Transformer for medical image segmentation**. *arXiv* 2021.
18. Pathan AK, Bond J, Gaskin RE: **Sample preparation for SEM of plant surfaces**. *Mater Today* 2010, **12**(supp-S1):32-43.
19. Yang Y, Li R, Qi M: **In vivo analysis of plant promoters and transcription factors by**

agroinfiltration of tobacco leaves. *Plant J* 2000, **22**(6):543-551.
20. Taha AA, Hanbury A: **Metrics for evaluating 3D medical image segmentation: analysis, selection, and tool**. *BMC Med Imaging* 2015, **15**(1):29.
21. Thai TT, Ku K-B, Le AT, Oh SSM, Phan NH, Kimm I-J, Chung YS: **Comparative analysis of stomatal pore instance segmentation: Mask R-CNN vs. YOLOv8 on Phenomics Stomatal dataset**. *Front Plant Sci* 2024, **15**:1414849.
22. Avzalov DR, Arif MAR, Komyshev EG, Koval VS, Börner A, Afonnikov DA: **Analysis of coat texture characteristics of bread wheat grains obtained from digital images**. *Front Plant Sci* 2025, **16**:1659548.
23. Haralick RM, Shanmugam K, Dinstein I: **Textural Features for Image Classification**. *IEEE Trans Syst Man Cybern* 1973, **SMC-3**(6):610-621.
24. Lantuejoul C, Maisonneuve F: **Geodesic methods in quantitative image analysis**. *Pattern Recognit* 1984, **17**(2):177-187.
25. Jarvis MC, Briggs SPH, Knox JP: **Intercellular adhesion and cell separation in plants**. *Plant Cell Environ* 2003, **26**(7):977-989.
26. Yuan J, Yang L, Yu P, Tang N, Liu L, Wang W, Wang P, Yang Q, Guo S, Li J: **Comparison and development of scanning electron microscope techniques for delicate plant tissues**. *Plant Sci* 2024, **340**:111963.
27. Talbot MJ, White RG: **Methanol fixation of plant tissue for Scanning Electron Microscopy improves preservation of tissue morphology and dimensions**. *Plant Methods* 2013, **9**(1):36.
28. Wang X, Qiao X, Meng B, Yao M, Liu Y, Zhang X, Botella JR, Wang W, Guo S: **The transcription factors ZmFAMA and ZmSCRM2 form a heterodimeric complex to regulate stomatal development in maize**. *J Exp Bot* 2025, **76**(22):6868-6880.